Ground Support 2026 - D Cumming-Potvin & J Wesseloo (eds.)
© 2026 Australian Centre for Geomechanics, Perth
doi:10.36487/ACG_repo/2625_46

Case studies of strainburst demand assessment

Alex Rigby [a,*], Moe Moridi [b], Farhan Hafeez [b], Dmitriy Malovichko [a], Peter Konrad Kaiser [c]

[a] *Institute of Mine Seismology, Australia*

[b] *Evolution, Australia*

[c] *GeoK Inc., Canada*

Abstract

During a tunnel strainburst, there is a rapid stress fracturing and bulking of rock, which imposes a simultaneous displacement and energy demand on the support system. The strainburst also constitutes a seismic source/event, the low-frequency radiation of which will be dominated by convergence of the surrounding rock mass into the tunnel, leading to a crush-type mechanism. Unlike cases of shakedown, it is not appropriate to estimate strainburst demand based on the intensity of ground motion (e.g. peak ground velocity/peak particle velocity) calculated from the size (potency, energy, or magnitude) of this event and its distance to tunnels. Instead, the fracturing/bulking process should be assessed more directly, which can be done by using a combination of geomechanical and seismic data. This paper presents such assessments for 2 case studies from a Western Australian hard rock mine. In each case, the estimated strainburst demand is also compared with the remnant capacity of the installed ground support. Performing such assessments on past events helps to better understand the demand that could be posed by future strainbursts, which can be used to guide support selection/design.

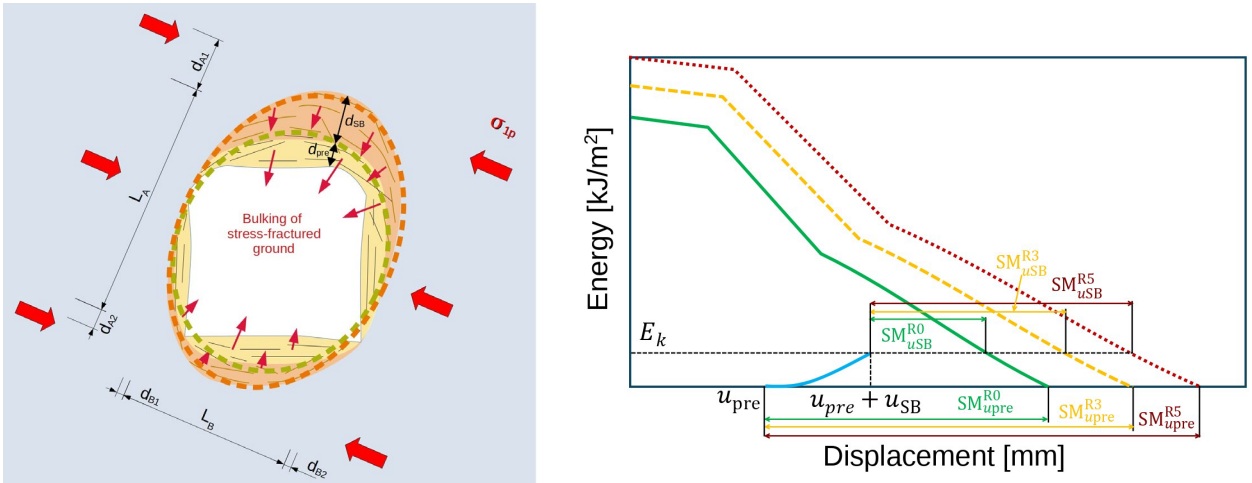
Keywords: *strainburst demand, remnant support capacity, rockburst hazard*

1 Introduction

A schematic illustration of a strainburst is shown in Figure 1a. Prior to a burst, there is a pre-existing damaged zone (shown in yellow) of depth d_{pre} that has accumulated by static and dynamic loading. The bulking of this damaged rock imposes a displacement demand u_{pre} on the support system. During a strainburst, the damaged zone rapidly expands by a depth d_{SB} to include the orange region. The bulking of this rock imposes an additional displacement u_{SB} and kinetic energy demand E_k on support. Following the approach of deformation-based support design (Kaiser & Moss 2022), strainburst demand (blue) can be compared graphically with the remnant capacity of the support system (green), as shown in Figure 1b. This comparison can be made quantitatively through calculation of the displacement safety margins $\mathrm{SM}_{u\mathrm{pre}}^{R0}$ and $\mathrm{SM}_{u\mathrm{SB}}^{R0}$ shown in Figure 1b, which give the remaining displacement capacity prior to and during a strainburst, respectively (Rigby et al. 2026b).

If strainburst demand exceeds the support system's remnant capacity by a small amount, then damage is expected, but not necessarily complete failure of the support system. Rather, if the areal/surface support is robust, localised failure of support elements will result in the transfer of load to neighbouring elements. In general, it can be expected that additional displacement beyond the design (R0) capacity will result in increasing levels of damage to the support system. To approximate this, it has been proposed by Rigby et al. (2026b) to also compare demand with damage thresholds for R3 (moderate) and R5 (severe) damage, which are offset in displacement relative to the design capacity. These are shown in orange and red in Figure 1b, respectively.

* Corresponding author. Email address: alex.rigby@imsi.org



(a) (b)

Figure 1 (a) View looking down a tunnel's axis. Prior to a strainburst, there is a pre-existing damaged zone shown in yellow with a depth d_{pre}. During a strainburst, the damaged zone rapidly expands by a depth d_{SB} to include the orange region. Red arrows indicate displacement that occurs during a strainburst; (b) Energy-displacement plot showing the demand path (blue), which is compared with the design (R0) remnant capacity of the ground support (green) as well as the R3 and R5 damage thresholds (orange and red, respectively)

Determining the demand path for a given strainburst requires estimating the pre-burst displacement u_{pre}, strainburst displacement u_{SB}, and kinetic energy E_k (Kaiser & Moss 2022; Rigby et al. 2026b). The pre-burst displacement can be calculated as

$$u_{\mathrm{pre}} = \mathrm{BF} d_{\mathrm{pre}} + u_{\mathrm{init}} \tag{1}$$

where:

BF = bulking factor

d_{pre} = pre-burst depth of damage (see Figure 1a)

u_{init} = initial/installation displacement of ground support.

The additional displacement demand imposed during a strainburst is

$$u_{\mathrm{SB}} = \mathrm{BF} d_{\mathrm{SB}}, \tag{2}$$

where d_{SB} is the depth of the strainburst (see Figure 1a). The total energy demand (per unit area) during a strainburst can be obtained as the sum

$$E_k = E_{\mathrm{bdn}} + E_{\mathrm{SB}} \tag{3}$$

where

$$E_{\mathrm{bdn}} = \frac{1}{2} \rho d_{\mathrm{pre}} v_{\mathrm{SB}}^2 \tag{4}$$

is the energy of the burden ('bdn') generated by the movement of rock that failed prior to the strainburst and

$$E_{\mathrm{SB}} = \frac{1}{2} \rho d_{\mathrm{SB}} \left(\frac{v_{\mathrm{SB}}}{2}\right)^2 \tag{5}$$

is the kinetic energy of the strainbursting volume. In Equations 4 and 5, ρ is the rock mass density and

$$v_{\mathrm{SB}} = \frac{u_{\mathrm{SB}}}{t_{\mathrm{SB}}} \tag{6}$$

is the velocity at the front of the strainburst volume. The duration of the strainburst t_{SB} can be estimated from seismic waveforms (Malovichko 2022). A more detailed explanation of the demand calculation is given by Rigby et al. (2026b).

This paper presents case studies of damaging strainbursts that occurred at a Western Australian mine. In each case, values of pre-existing depth of damage d_{pre}, BF, strainburst depth d_{SB}, and duration of strainbursting t_{SB} are estimated from available seismic and geotechnical data to assess demand as outlined above. This demand is compared with the remnant capacity of the installed support, which is calculated from its constituent elements (bolts, shotcrete, mesh, etc).

2 Case 1

2.1 Data overview

As shown in Figure 2a, this case consists of 3 events that occurred near a tunnel: Event 1 – a m_W 0.9 at 05:35:29 on 14 October 2022, Event 2 – a m_W 1.3 at 09:14:47 on 14 October 2022, and Event 3 – a m_W 1.1 at 08:33:58 on 16 October 2022. The red dipoles in Figure 2a indicate the P-axis directions, which are sub-horizontal and approximately orthogonal to the tunnel direction. The source types of these events are presented in the Hudson plot of Figure 2b. Event 1 lies near the boundary of the crush- and slip-type regions (Malovichko & Rigby 2022), Event 2 is slip type, and Event 3 is crush type.

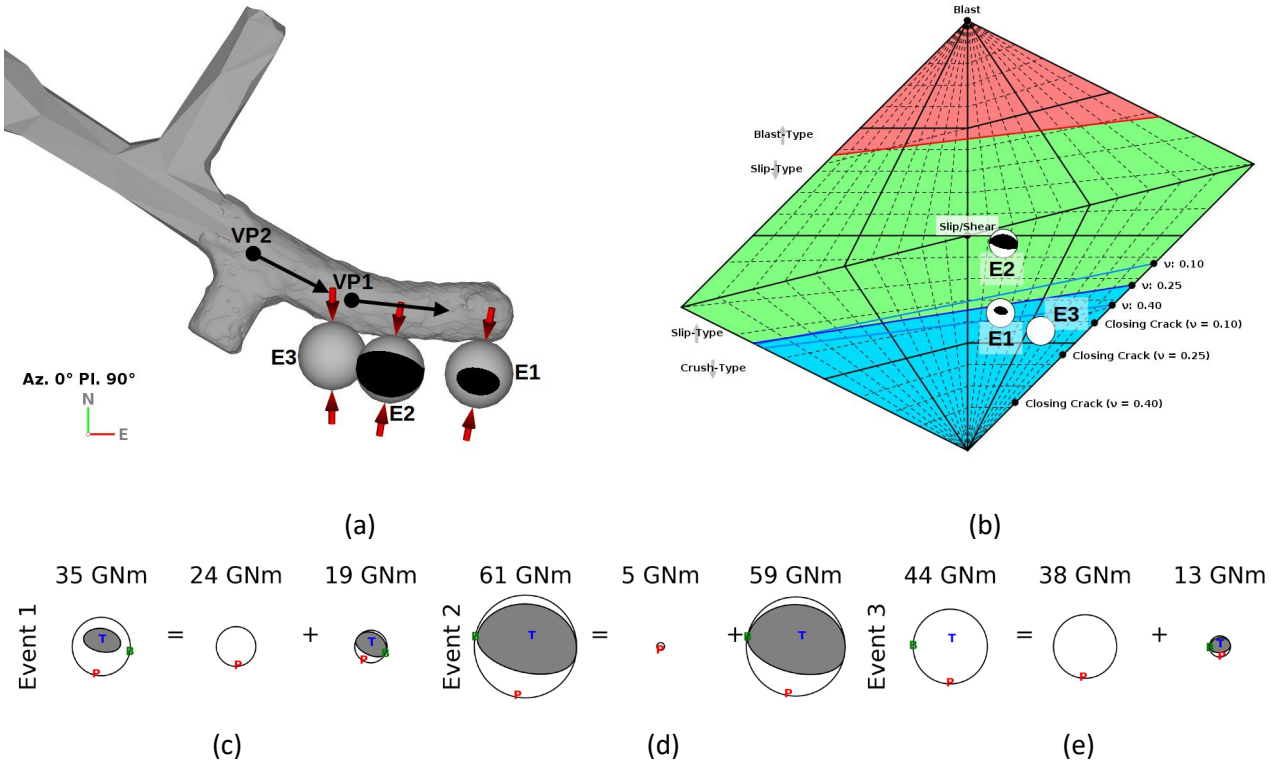
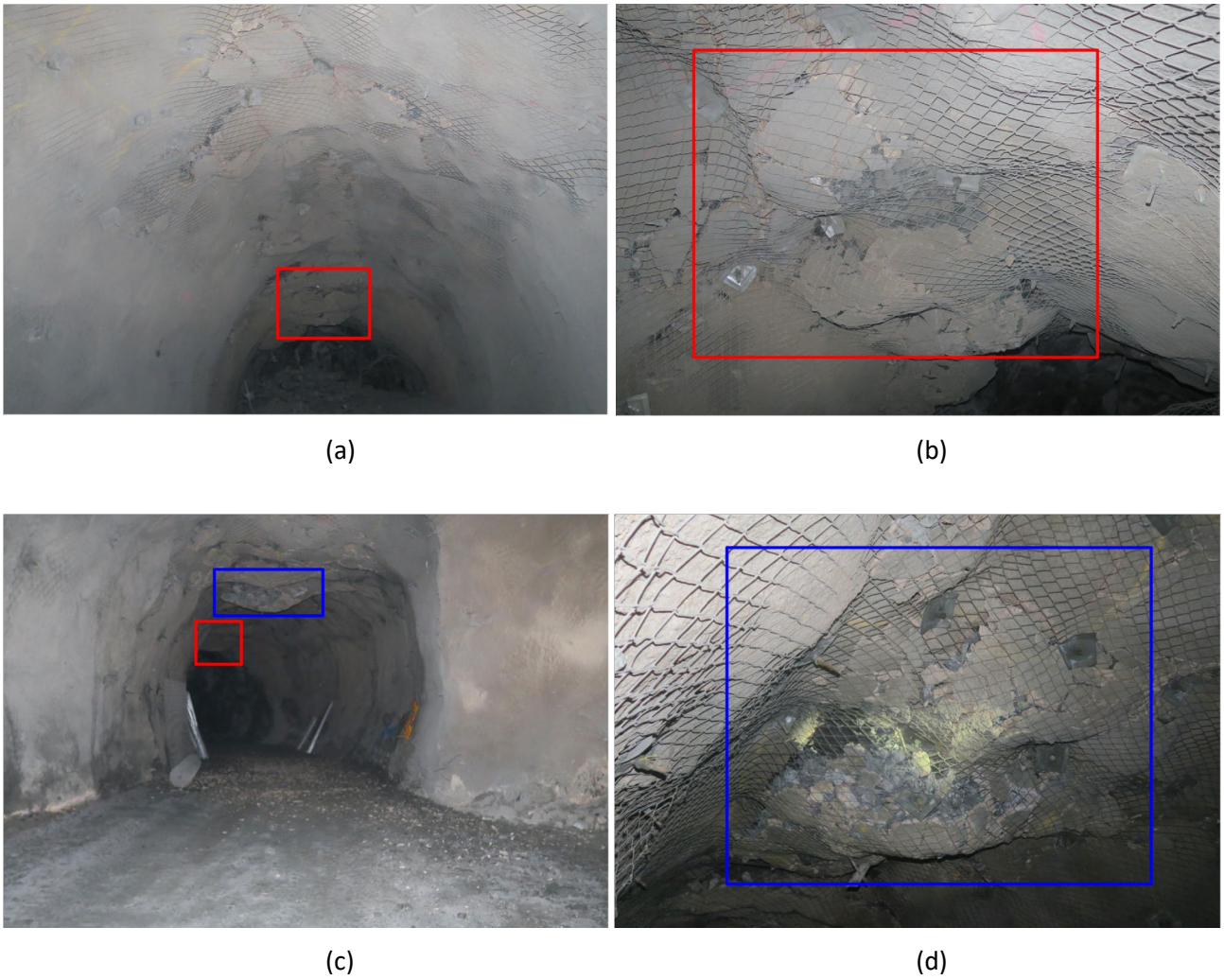


Figure 2 (a) Plan view showing Case 1 events of interest as beachballs. The red dipoles indicate the P-axis direction for each event. The black arrows indicate the viewpoints of photos shown in Figure 3; (b) Hudson diagram showing the source types of the 3 events; (c) Decomposition of the moment tensor for Event 1 (E1) into closing-crack and double-couple components. The scalar moment of each component is listed above the corresponding beachball diagram; (d) Same for Event 2 (E2); (e) Same for Event 3 (E3)

Figure 3a shows a photo taken on 14 October after Event 1 and Event 2, which has been taken from Viewpoint 1 (VP1) as indicated in Figure 2a. There was damage in the back extending approximately 17 m along the tunnel, which consisted of fracturing of fibre-reinforced shotcrete (FRS) and deformation of the

mesh and bolts. The most severe damage, which is outlined in red, occurred along approximately 5 m of the tunnel back near the face. A close-up of this damage is shown in Figure 3b, which has been categorised as R3 damage according to the scale of Rigby et al. (2026b). Figure 3c shows a photo taken on 16 October after Event 3, which has been taken from Viewpoint 2 (VP2) as indicated in Figure 2a. The existing section of R3 damage is outlined in red. A new section of R4 damage, which extended along approximately 8 m of the tunnel back, is outlined in blue, and a close-up is given in Figure 3d.



(a) (b)

(c) (d)

Figure 3 (a) Photo of damage in the tunnel back taken on 14 October from Viewpoint 1 as indicated in Figure 2a. The most severe damage is outlined in red; (b) Close-up of the most severe damage; (c) Photo of damage in the tunnel back taken on 16 October from Viewpoint 2 as indicated in Figure 2a. The most severe damage observed on 14 October is outlined in red. A section of the back with the most significant new damage is outlined in blue; (d) Close-up of the new damage

2.2 Remnant support-system capacity

The installed support system is described in Figure 4. In the back of the tunnel (where the damage was observed), it is composed of 50 mm FRS, 80/4 Geobrugg chainlink mesh, and 2.4 m × 20 mm Posimix bolts with a centrally positioned 1.2 m debonded section. The ring spacing is RS = 1.2 m and the bolt spacing is BS = 1.2 m. There is also a single ring of MDX bolts installed at the leading edge, but these do not contribute significantly to capacity and are therefore excluded from calculations for simplicity.

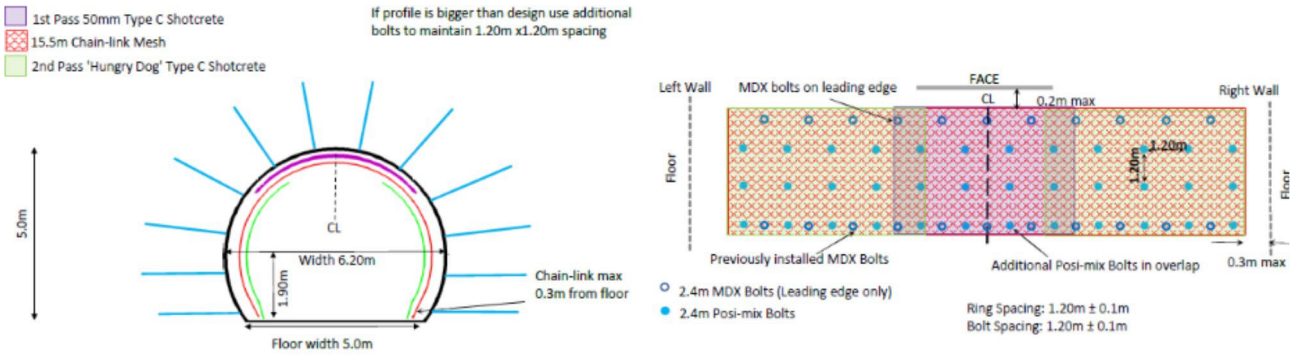


Figure 4 (a) Section view of support installed in Case 1 tunnel; (b) Unrolled plan view of same event

For the purposes of capacity calculation, it is assumed that the Posimix bolts are installed at an initial displacement of u_{init} = 20 mm and that they behave perfectly plastically. Table 1 lists the adopted values of maximum force F_m and ultimate displacement u_{ult} for direct (D) (near the bolt plate) and indirect (ID) (internal to the rock mass) load. It is assumed that half of loading is direct and the other half indirect, which gives F_m = 240 kN and u_{ult} = 92.5 mm. The dashed orange line in Figure 5a gives the force-displacement relation for the Posimix bolts, which is normalised to the square of the effective spacing ES^2 = BS × RS = 1.44 m^2 (i.e. it is pressure). The red curve in Figure 5a gives the force-displacement relation for the bolting system as a whole, which is equal to that of the Posimix bolts in this case because only a single type of bolt is considered.

The areal-support elements (FRS and mesh) are assumed to have elastic (linear) force-displacement curves based on approximation as a simply supported beam. A simplifying assumption is made that the displacement of the areal-support elements (i.e. the central deflection) is equal to that of the bolts. Table 2 lists the adopted values of bending stiffness k for a reference spacing (beam length) of 1.2 m, rupture/punch-through force F_r, and allowable displacement u_{all}, which is the maximum operationally acceptable displacement. The dashed blue line in Figure 5a gives the force-displacement curve for the FRS, which is assumed to be installed at 0 mm displacement and reaches a rupture pressure of F_r/ES^2 = 14 kN/m^2 at a displacement of 33 mm. The dotted blue line gives the force-displacement curve for the Geobrugg mesh, which is installed at 20 mm along with the bolts. The Geobrugg mesh does not contribute to the total force-displacement curve of the areal-support system (solid green line) beyond a displacement of approximately 110 mm (when the bolts reach capacity). Summing the force-displacement curves for the bolts and areal-support gives the black 'total' curve in Figure 5a.

Table 1 Assumed values of maximum force F_m and ultimate displacement u_{ult} for bolts under direct (D) and indirect (ID) loading

Bolt	F_m(D) (kN)	u_{ult}(D) (mm)	F_m(ID) (kN)	u_{ult}(ID) (mm)
2.4 m x 20 mm Posimix	240	45	240	140
2.4 m x 47 mm MDX	220	40	220	80

Table 2 Assumed values of bending stiffness k, rupture force F_r, and allowable displacement u_{all} for areal-support elements

Element	k (MN/m)	F_r (kN)	u_{all} (mm)
50 mm FRS	0.6	20	50
80/4 Geobrugg mesh	0.12	120	175
4GA (5.6 mm) weld mesh	0.24	45	175

Figure 5b presents the remnant capacity of the support system in black, which shows that the installed energy capacity of 16 kJ/m^2 reduces to zero at a displacement of approximately 110 mm when the bolts reach capacity. In cases where the areal support is not the weakest link, it can be expected that exceeding the design capacity of the support system will not lead to total failure as discussed in Section 1. Instead, greater damage is expected with increasing displacement beyond the design (R0) capacity. Thresholds for R3 and R5 damage have been calculated by assuming that an additional displacement of Δu_{R3} = 30 mm and Δu_{R3} = 60 mm is required to reach these levels of damage. This gives the orange and red force-displacement curves in Figure 5c (corresponding to R3 and R5, respectively), which then yield the thresholds shown in Figure 5d.

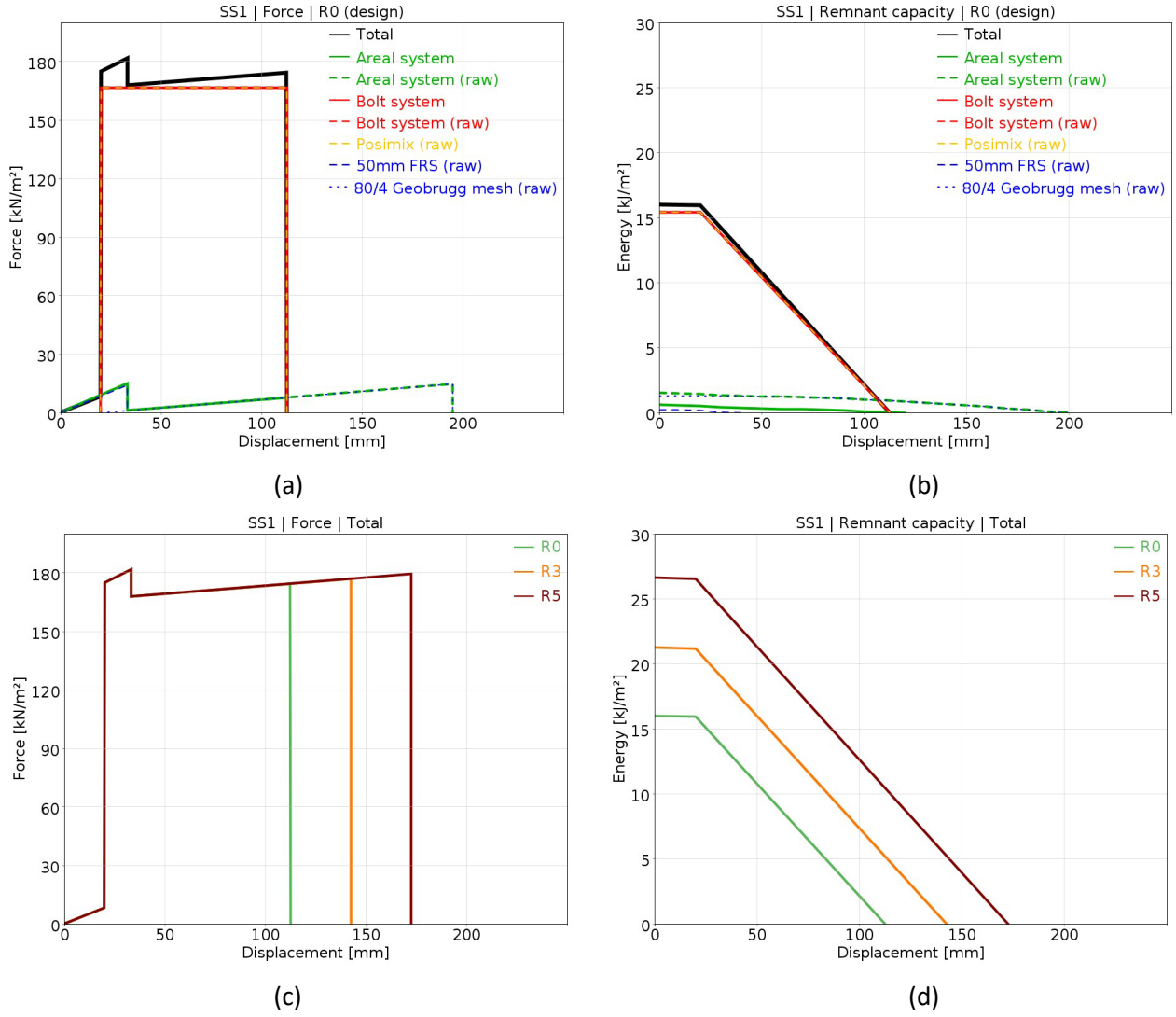


Figure 5 (a) Design (R0) force-displacement curves for the Case 1 support system based on the parameters listed in Tables 1 and 2; (b) Corresponding remnant-capacity curves; (c) Force-displacement curves for different damage thresholds; (d) Corresponding remnant-capacity thresholds

2.3 Event 1

The damage observed on 14 October near the face (see Figures 3a and 3b) followed Events 1 and 2 as defined in Section 2.1. Given that Event 2 has a near-pure slip-type mechanism (see Figure 2b), it can be interpreted as an episode of slip along a pre-existing weakness. Event 1 has a mechanism composed of slip-type and crush-type content. This crush-type content can be interpreted as an episode of dynamic stress fracturing in

the back/floor of the tunnel, which is consistent with the observed damage. Following this logic, this section assumes that the demand imposed by Event 1 is the sole cause of damage.

2.3.1 Pre-existing depth of damage

In the absence of any direct observations of pre-existing depth of damage d_{pre} (e.g. from borehole camera observations), an estimate can be made based on stress-level index $\text{SLI} = \sigma_{\max}/\text{UCS}^*$. Here, $\sigma_{\max}$ is the maximum tangential stress around an equivalent circular tunnel of radius a, and UCS^* is the 'calibrated' unconfined compressive strength. If no field observations of d_{pre} are available, then it is suggested by Rigby et al. (2026b) to use the 75-th percentile value of UCS from lab testing to reduce bias from low-strength/defected samples, which gives a value of UCS^* = 184 MPa in this case. Given that the tunnel of interest is not near any large-scale excavations (e.g. stopes), it is appropriate to estimate $\sigma_{\max}$ from in situ stress. At the depth of the tunnel of interest, σ_1 = 42 MPa and is oriented north-south, σ_2 = 29 MPa and is oriented east-west, and σ_3 = 19 MPa is oriented vertically. The maximum stress induced around a circular tunnel is $\sigma_{\max} = 3\sigma_{1p} - \sigma_{3p}$, where σ_{1p} and σ_{3p} are the maximum and minimum stresses in a plane orthogonal to the tunnel direction, respectively. In this case, the tunnel horizontal and at an azimuth of 100° (approximately orthogonal to σ_1), giving σ_{1p} = 41 MPa ≈ σ_1 and σ_{3p} = 19 MPa = σ_3. This results in values of $\sigma_{\max}$ = 105 MPa and SLI = 0.57.

Based on the modelling results of (Perras & Diederichs 2016), the extreme depth of failure can be estimated from SLI as

$$d_f^e = \begin{cases} 0.58a\left(\frac{\text{SLI}}{0.43} - 1\right)^{0.65} & \text{for SLI} > 0.43 \\ 0 & \text{otherwise} \end{cases} \quad (7)$$

Taking a = 3.1 m based on the design profile shown in Figure 4, this gives d_f^e = 0.85 m. Note that this is the extreme (worst-case) depth of failure for an unsupported tunnel. In practice, it can be expected that only a fraction q_{pre} of d_f^e will be realised as pre-existing damage on average (Kaiser 2016; Rigby et al. 2026b). Ideally, q_{pre} would be calibrated using a set of field observations, which aren't available in this case. As such, a value of q_{pre} = 20% is selected based on experience, which gives $d_{\text{pre}} = q_{\text{pre}} d_f^e$ = 0.17 m. This best-estimate value of d_{pre} is subject to considerable uncertainty due to the assumptions underlying its calculation and the uncertainty in the parameters used. To at least somewhat account for this in subsequent demand calculations, it is assumed that d_{pre} follows a triangular distribution with a minimum value of 0.5 × 0.17 m = 0.08 m, nominal/modal value of 0.17 m, and maximum value of 1.5 × 0.17 m = 0.26 m, which is denoted as d_{pre} = tri(0.08,0.17,0.26) m.

2.3.2 Bulking factor

When stress fracturing occurs in rock around a tunnel, geometric inconsistencies between the fractured pieces result in an increase in volume. This 'bulking' results in a displacement/convergence of the excavation surface, which loads the installed ground support. The ratio of this displacement to the depth of fracturing is given by the bulking factor (BF), which is dependent on factors including rock properties, stress level, and particularly the confining stress (support pressure) imposed by the support system (Kaiser et al. 1996). Note that not all displacement of ground support is directly due to bulking. For example, it can be seen in Figure 3b that the large displacements between bolts are primarily due to the gravitational loading of bagged material, which is causing the mesh to sag.

When yielding support is installed, a value of BF = 5 ± 1% is suggested by Kaiser et al. (1996). For the mine considered in this paper, site-specific BF estimates have been made using LiDAR data (Rigby et al. 2026a). Using data from the case presented in Section 3, a of BF = tri(3.9,4.4,5.8)% was estimated through careful comparison of displacement and depth of fracturing in a section of tunnel where displacement was expected to primarily be the result of bulking (rather than gravitational loading). For the analysis of this case, the same BF distribution is used.

2.3.3 Depth of strainbursting

Figure 1a shows a schematic of strainbursting around a tunnel, with the pre-existing damaged zone (yellow) rapidly expanding to include the orange region, each of which are approximated by ellipses. This dynamic expansion produces seismic radiation, the low-frequency content of which is dominated by the overall convergence of the surrounding rock mass into the excavation (rather than by small-scale episodes of shear and tensile rupture within the stress fracturing volume) (Malovichko 2020; Malovichko & Rigby 2022). As a result, the moment tensor for a seismic event corresponding to tunnel strainbursting has a crush-type mechanism that provides information about the geometry of the damaged zone's growth. In particular, the scalar moment can be expressed as

$$M_0 = 2\frac{1-\nu}{1-2\nu}|\sigma_{1p}|L_3\left(L_A + \frac{1}{2}d_A\right)d_A \tag{8}$$

where ν is Poisson's ratio, σ_{1p} is the in-plane maximum principal stress, L_3 is the extent of damage along the tunnel, L_A is the effective diameter of the tunnel prior to the event, and d_A is the effective increase in this diameter (Malovichko & Rigby 2022). As shown in Figure 1a, this increase in diameter can be distributed across both sides of the tunnel, with $d_A = d_{A1} + d_{A2}$.

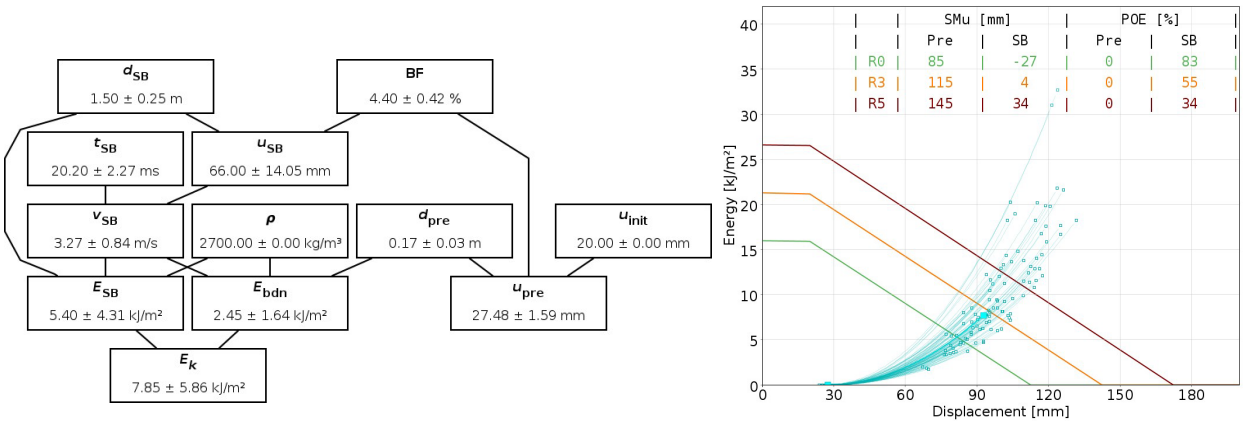
For the case at hand, Equation 8 can be used to estimate d_A. Importantly, the scalar moment M_0 used should correspond to the event's crush-type component, which can be determined using the decomposition methodology of Rigby (2024). Figure 2c shows a decomposition of Event 1's mechanism into closing-crack and double-couple (i.e. crush- and slip-type) components, with the corresponding scalar moments listed above each. Taking M_0 = 24 GNm, ν = 0.25, $|\sigma_{1p}|$ = 41 MPa (based on in situ stress and tunnel orientation), L_3 = 5 m (corresponding to the section of most significant damage near the face), and L_A = 6.54 m (based on the design radius of a = 3.1 m and the value of d_{pre} = 0.17 m estimated in Section 2.3.1) gives d_A = 4.45 m. Assuming this increase is evenly distributed across the back and floor of the tunnel gives $d_{A1} = d_{A2}$ = 2.22 m. This can be considered as an upper bound on the depth of strainbursting d_{SB} because, as shown in Figure 3a, damage extended along approximately 17 m of the tunnel's back (not just along the 5 m near the face). A lower bound on d_{SB} can be estimated by assuming that the depth of fracturing was evenly distributed along this 17 m section by taking L_3 = 17 m in Equation 8, which gives $d_{A1} = d_{A2}$ = 0.78 m. Based on these 2 estimates, a triangular distribution of d_{SB} = tri(0.78,1.50,2.22) m is adopted for this case, with the nominal value just being the mean of the 2 bounds.

2.3.4 Duration of strainbursting

Following the methodology of Malovichko (2022), the strainburst duration t_{SB} can be estimated from seismic data. This requires an estimate of the origin time t_0 (the time at which fracturing initiates), which is inferred when locating an event, and the centroid time t_c (the time at which half the seismic moment has been released), which can be inferred as part of a full-waveform mechanism inversion. From these 2 times, the strainburst duration can be calculated as $t_{\text{SB}} = 2(t_c - t_0)$. For this event, a best estimate of t_{SB} = 20.2 ms has been made using this approach. There is some uncertainty in the centroid time used to make this estimate, with different values giving similar fits in the full-waveform inversion. Based on values giving similar fits, a distribution of t_{SB} = tri(15.2,20.2,26.6) ms is used for this case.

2.3.5 Strainburst demand

Using the nominal (best-estimate) values of d_{pre} = 0.17 m (see Section 2.3.1), BF = 4.4% (see Section 2.3.2), and u_{init} = 20 mm (see Section 2.2), the pre-burst displacement can be calculated from Equation 1 as u_{pre} = 27 mm. This value is listed in the bottom right of the flow chart of Figure 6a and defines the start point of the nominal demand path in Figure 6b (thick cyan line). In addition to this deterministic estimate of u_{pre}, the triangular distributions d_{pre} = tri(0.08,0.17,0.26) m and BF = tri(3.9,4.4,5.8)% have been sampled 100 times to give 100 different realisations of u_{pre}, which have a standard deviation of 1.6 mm as listed in Figure 6a. These realisations define the start points of the 100 'sample' demand paths in Figure 6b (thin cyan lines).



(a) (b)

Figure 6 (a) Flow chart of demand calculation for Event 1 of Case 1; (b) Demand versus capacity plot for the same event

From Equation 2, the strainburst displacement has been calculated as u_{SB} = 66 ± 14 mm from the distributions d_{SB} = tri(0.78,1.50,2.22) m (see Section 2.3.3) and BF = tri(3.9,4.4,5.8)%. When added to the pre-burst displacement, this gives the displacement at demand path endpoints shown in Figure 6b. From Equation 6, the strainburst velocity is v_{SB} = 3.3 ± 0.8 m/s. For an assumed density of ρ = 2700 kg/m^3, this yields values of E_{bdn} = 2.5 ± 1.6 kJ/m^2 (see Equation 4) and E_{SB} = 5.4 ± 4.3 kJ/m^2 (see Equation 5) for the burden and strainbursting volumes, respectively. These sum to give a total kinetic energy of E_k = 7.9 ± 5.9 kJ/m^2 (see Equation 3), which is the energy at the demand-path endpoints shown in Figure 6b. Note that the uncertainty in the energy demand is significantly more uncertain than for the displacement demand, which is a result of compounding uncertainty in input parameters.

It can be seen in Figure 6b that the nominal demand path (thick cyan line) exceeds the design capacity (R0 threshold) for the support system, which is reflected in the negative strainburst safety margin $\mathrm{SM}_{u\mathrm{SB}}^{R0}$ = −27 mm listed in Figure 6b (measured horizontally from the demand path end point to the R0 curve). However, it does not exceed the R3 damage threshold, with the corresponding safety margin $\mathrm{SM}_{u\mathrm{SB}}^{R3}$ = 4 mm being (barely) positive. This means that, based on the best estimates of demand inputs, R1-R2 damage is expected, which is less severe than the R3-level damage that was observed. The scatter in the sample path endpoints indicates the significant uncertainty in the demand imposed on the support. By counting the number of sample paths exceeding each damage threshold, the probability of at least minor (R0) damage is 83%, moderate (R3) damage is 55%, and severe (R5) damage is 34%. Put differently, this corresponds to a 17% chance of no damage, 28% chance of R1-R2 damage, 21% chance of R3-R4 damage, and a 34% chance of R5 damage.

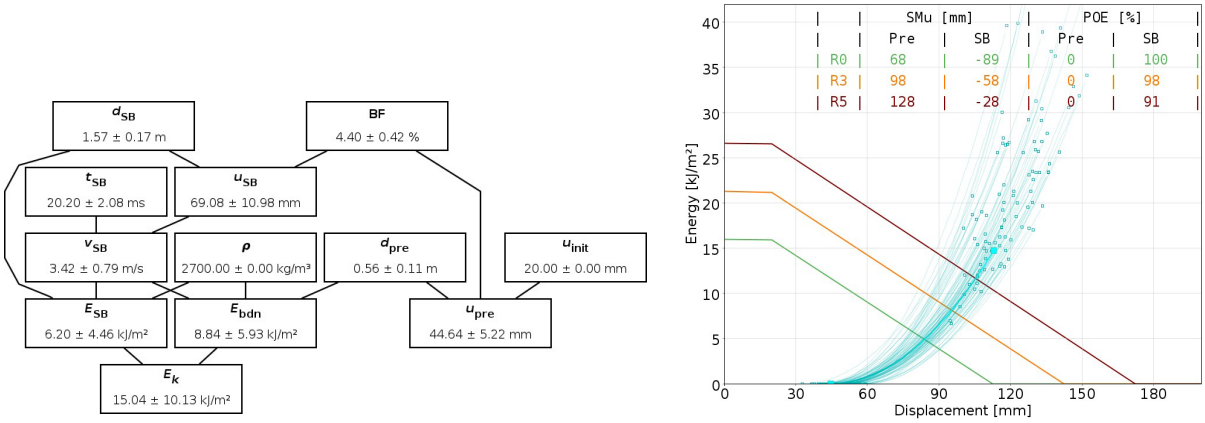
2.4 Event 3

For Event 3, which is associated with the damage outlined in blue in Figures 3c and 3 d, the pre-existing depth of damage d_{pre} is due to both static stress fracturing and also dynamic stress fracturing associated with Event 1. In such cases, d_{pre} can be estimated as $d_{\mathrm{pre}} = q_{\mathrm{pre}} d_f^e + \sum d_{\mathrm{SB}}$, where $\sum d_{\mathrm{SB}}$ is the cumulative depth of dynamic stress fracturing from previous events (Malovichko 2022; Rigby et al. 2026b). For the scenario considered in Section 2.3.3, in which Event 1 extended only along the 5 m of most severe damage near the face, it would be reasonable to take $\sum d_{\mathrm{SB}}$ = 0 m for Event 3. Alternatively, for the scenario where Event 1 extended evenly along 17 m of tunnel, $\sum d_{\mathrm{SB}}$ = 0.78 m. Based on these bounds, a value of $\sum d_{\mathrm{SB}}$ = 0.39 m is used here, which gives d_{pre} = 0.56 m when added to the same $q_{\mathrm{SB}} d_f^e$ = 0.17 m used for Event 1. To account for the uncertainty in this estimate, a distribution of d_{pre} = tri(0.28,0.56,0.84) m is adopted based on an assumed ±50% variance.

Following the same approach as Section 2.3.3, an estimate of strainburst depth d_{SB} is made by considering 2 extreme scenarios. In the first scenario, it is assumed that Event 3 extended along only the L_3 = 8 m section of

tunnel where the most severe damage was observed. Along with values of M_0 = 38 GNm (see Figure 2e), ν = 0.25, $|\sigma_{1p}|$ = 41 MPa, and L_A = 7.3 m (based on the design shape and assumed d_{pre}), Equation 8 yields an estimate of d_{A1} = d_{A2} = 2.06 m. Alternatively, if it is assumed that Event 3 extended along L_3 = 17 m of tunnel, then d_{A1} = d_{A2} = 1.08 m. Based on these estimates, a distribution of d_{SB} = tri(1.08,1.57,2.06) m is adopted for Event 3. The bulking factor distribution BF = tri(3.9,4.4,5.8)% used for Event 1 is also used for Event 3. Following the procedure described in Section 2.3.4, the strainburst duration is taken as t_{SB} = tri(13.4,20.2,23.2) ms.

Using the inputs defined above, Figure 7a shows a flow chart of demand calculation, and Figure 7b compares demand and capacity in displacement-energy space. The estimated demand is higher than for Event 1, with 91% of samples exceeding the R5 damage threshold, meaning that complete failure of the support system is expected. This increase in demand compared to Event 1 is primarily due to the increase in pre-existing depth of damage d_{pre} (0.56 m compared to 0.17 m), which contributes to a larger pre-burst displacement u_{pre} (45 mm compared to 27 mm) and a significant increase to the burden kinetic energy E_{bdn} (8.8 kJ/m^2 compared to 2.5 kJ/m^2). While the observed damage was slightly more severe than for Event 1 (see Figures 3c and 3d), there was not a complete failure of the support system. This discrepancy can possibly be attributed to the conservative manner in which pre-existing burden is expected to contribute to energy demand. As given by Equation 4, the burden is expected to move uniformly as an incompressible volume at the strainburst velocity v_{SB}, loading the support system. In practice, if the burden of stress-fractured rock is compressible, it would have an average velocity less than v_{SB}, resulting in a reduced energy demand.



(a) (b)

Figure 7 (a) Flow chart of demand calculation for Event 3 of Case 1; (b) Demand versus capacity plot for the same event

3 Case 2

3.1 Data overview

As shown in Figure 8a, this case consists of 2 events that occurred near a tunnel on 22 December 2024: Event 1 – a m_W 1.0 at 12:34:26 and Event 2 – a m_W 1.1 at 12:37:08. Both had mechanisms composed of a combination of crush- and slip-type content (see Hudson plot in Figure 8b). Decompositions into closing-crack (crush) and double-couple (slip) components are shown in Figures 8c and 8d.

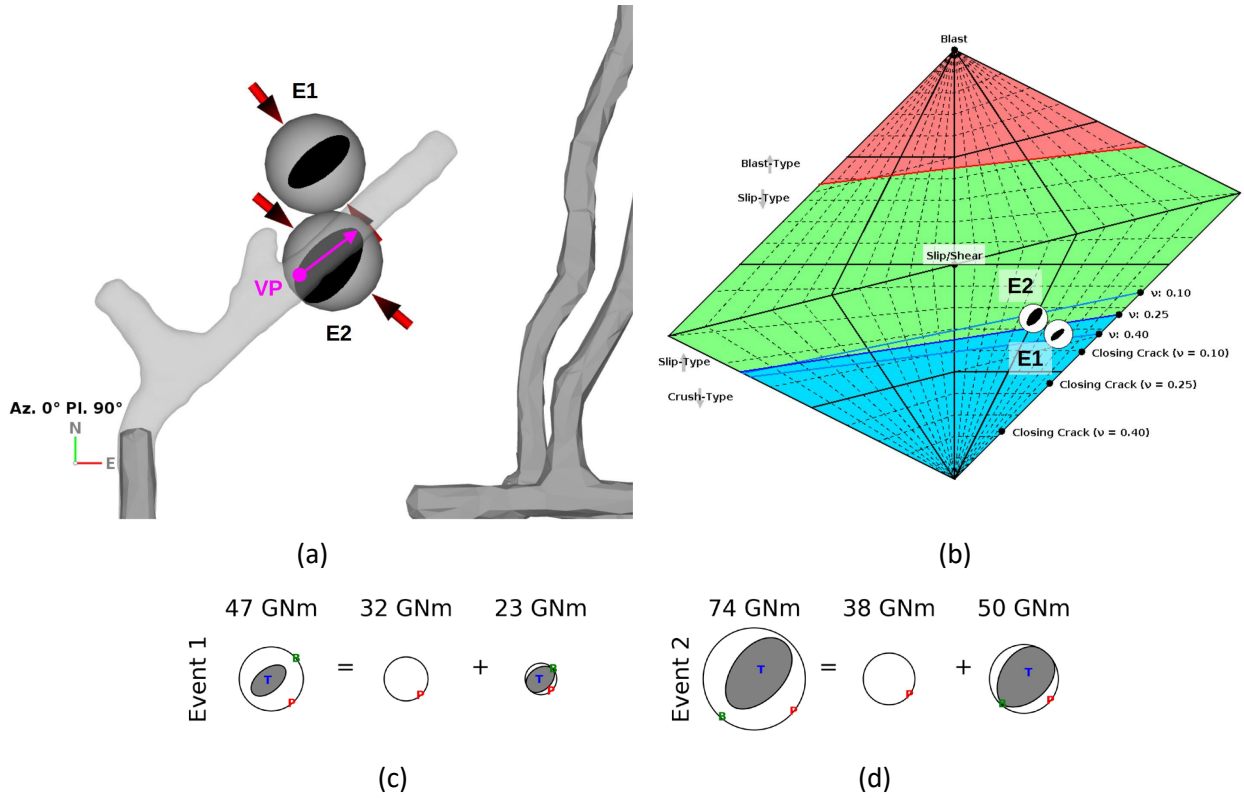


Figure 8 **(a) Plan view showing Case 2 events of interest as beachballs. The red dipoles indicate the P-axis direction for each event. The pink arrow indicates the viewpoint of the photo shown in Figure 9a; (b) Hudson diagram showing the source types of the 2 events; (c) Decomposition of the moment tensor for Event 1 into closing-crack and double-couple components. The scalar moment of each component is listed above the corresponding beachball diagram; (d) Same for Event 2**

Following the 2 events, damage was observed in the back of the tunnel as shown in the photo in Figure 9a, which was taken from the viewpoint indicated in Figure 8a. A section of bagged rock is outlined in red in Figure 9 with a close-up photo given in Figure 9b. In total, the damage extended along approximately 19 m of the tunnel back and was categorised as R3-R4.

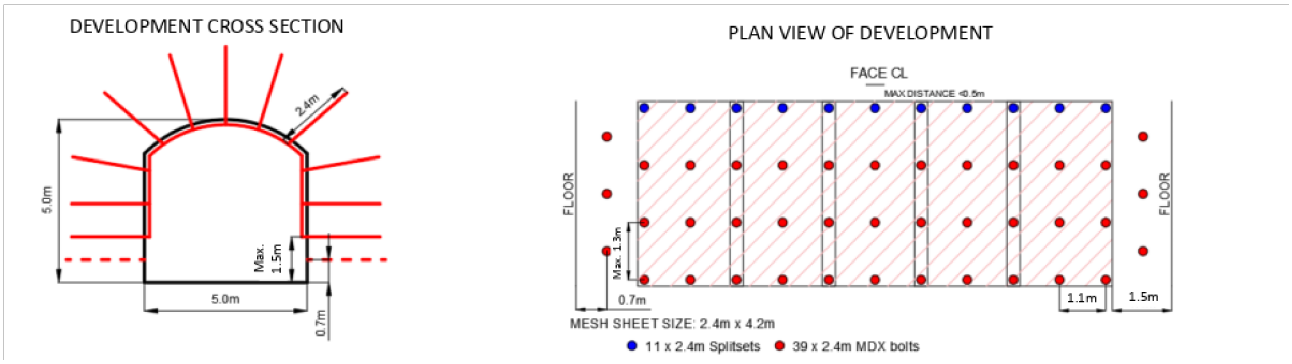


(a) (b)

Figure 9 **(a) Photo of damage in the tunnel back taken on 22 December 2024 from viewpoint as indicated in Figure 2a. A section of more severe damage is outlined in red; (b) Close-up of this section**

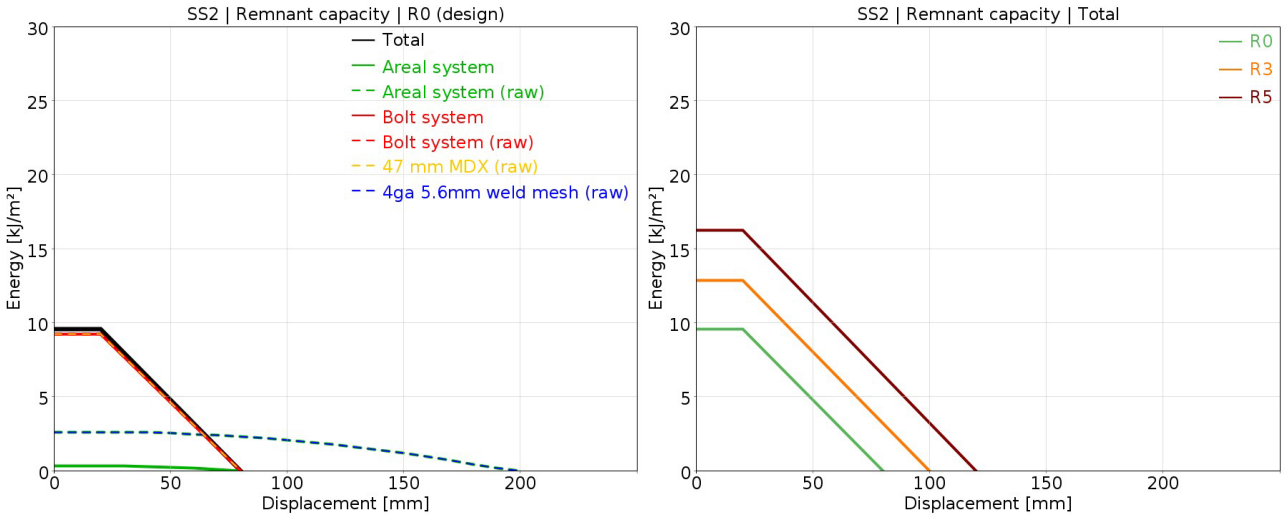
3.2 Remnant support-system capacity

The installed support system is shown in Figure 10, which is composed of 4GA (5.6 mm) weld mesh and 2.4 m × 47 mm MDX bolts installed with a ring spacing of 1.3 m and a bolt spacing of 1.1 m. Using the MDX and weld mesh parameters listed in Tables 1 and 2, respectively, the design remnant capacity of the support system has been determined following the method outlined in Section 2.2 and is shown in Figure 11a. The displacement and energy capacity is lower than for the Case 1 support system. The reduction in displacement capacity is due to the lower ultimate displacement assumed for the MDX bolts (40 mm versus 45 mm for Posimix under direct loading and 80 mm versus 140 mm under indirect loading). The reduction in energy capacity is due to a reduction in maximum bolt force (220 kN versus 240 kN for Posimix) and ultimate displacement, an increase in ring spacing (1.3 m versus 1.1 m for Case 1), and the absence of FRS. Figure 11b shows thresholds for R3 and R5 damage, which have been calculated using values of Δu_{R3} = 20 mm and Δu_{R5} = 40 mm.



(a) (b)

Figure 10 (a) Section view of support installed in Case 2 tunnel; (b) Unrolled plan view of the same



(a) (b)

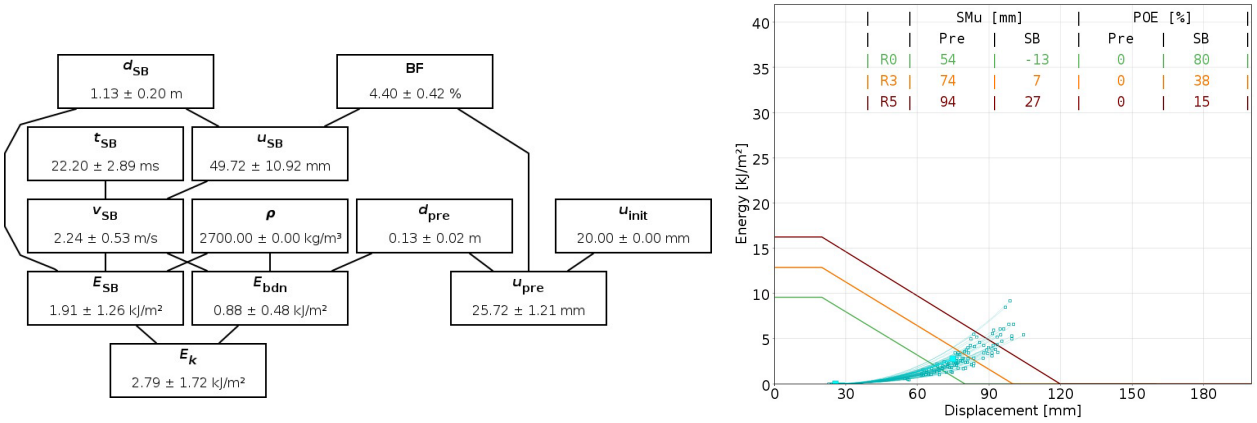
Figure 11 (a) Design (R0) remnant-capacity curve for the Case 2 support system based on the parameters listed in Tables 1 and 2; (b) Remnant-capacity thresholds

3.3 Event 1

The pre-existing depth of damage prior to Event 1 is calculated through the same empirical approach employed in Section 2.3.1. In this case, σ_{max} = 80 MPa and UCS* = 155 MPa, which gives a stress level index of SLI = 0.52. Using a value of a = 3.2 m (based on the size of a circle circumscribing the tunnel profile shown in

Figure 10), Equation 7 gives an extreme depth of failure of d_f^e = 0.65 m. Assuming q_{pre} = 20% yields an estimate of d_{pre} = 0.13 m. As with Case 1, this estimate is uncertain, so a triangular distribution of d_{pre} = tri(0.07,0.13,0.20) m is adopted based on a ±50% variation. Assuming that Event 1 extended along the entire 19 m of damaged tunnel and taking M_0 = 32 GNm, ν = 0.25, $|\sigma_{1p}|$ = 32 MPa, and L_A = 6.7 m yields a strainburst depth of d_{SB} = 1.13 m from Equation 8 (assuming d_A is evenly distributed across both the back and floor). This estimate is also quite uncertain (e.g. Event 1 may not have extended along the entire 19 m of damaged tunnel), so a triangular distribution of d_{SB} = tri(0.56,1.13,1.69) m is used, again based on an assumed ±50% variation. As for Case 1, a bulking-factor distribution of BF = tri(3.9,4.4,5.8)% is used, and a strainburst duration distribution of t_{SB} = tri(19.4,22.2,33.6) ms has been determined from full-waveform mechanism inversion.

Based on these estimated/selected distributions, Figure 12a gives a flow chart of demand calculations, and Figure 12b compares demand with capacity. The nominal demand path exceeds the design (R0) capacity, but not the R3 damage threshold, which indicates that (based on nominal/best-estimate parameters), R1 or R2 damage is expected. Looking at the 100 samples gives a slightly more nuanced view, with 80% exceeding the design (R0) capacity, 38% exceeding the R3 threshold, and 15% exceeding the R5 threshold.



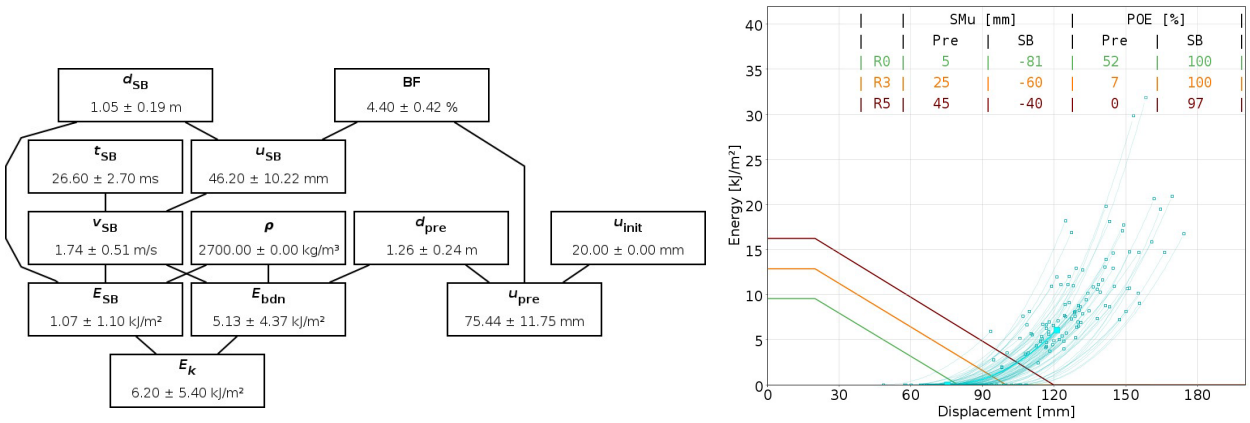
(a) (b)

Figure 12 (a) Flow chart of demand calculation for Event 1 of Case 2; (b) Demand versus capacity plot for the same event

3.4 Event 2

For Event 2, d_{pre} is assumed to be composed of the 0.13 m of estimated static fracturing in Section 3.3 as well as $\sum d_{\text{SB}}$ = 1.13 m as a result of Event 1. Assuming a ±50% variation, this gives a distribution of d_{pre} = tri(0.63,1.26,1.89) m. Taking L_3 = 19 m, M_0 = 38 GNm, ν = 0.25, $|\sigma_{1p}|$ = 32 MPa, and L_A = 8.9 m yields a strainburst depth of 1.05 m from Equation 8, which gives a distribution of d_{SB} = tri(0.52,1.05,1.58) m for an assumed ±50% variation. Again, BF = tri(3.9,4.4,5.8)%, and t_{SB} = tri(17.6,26.6,30.2) ms has been determined from full-waveform mechanism inversion.

Figure 13 presents a demand flow chart and comparison of demand with capacity for Event 2. The starting point of the nominal demand path is already very near to the design capacity, which is due to the previous demand of Event 1. The end point exceeds the R5 threshold, indicating that (based on best-estimate parameters) total failure of the support is expected. The sample demand paths indicate a 97% chance of R5 damage. These results are not consistent with the less severe R3-R4 damage observed. Again, this could possibly be attributed to the conservative way that burden is treated as discussed in Section 2.4. However, there are other possibilities for this discrepancy; for example, the damage may have been concentrated in the floor rather than split evenly between the floor and back as assumed here.



(a) (b)

Figure 13 (a) Flow chart of demand calculation for Event 2 of Case 2; (b) Demand versus capacity plot for the same event

4 Conclusion

Two cases of damaging strainbursts at a Western Australian mine have been presented. In each case, strainburst displacement and energy demand has been determined based on estimates of pre-existing depth of damage, strainburst depth, bulking factor, and strainburst duration. This demand has been compared with the remnant capacity of the ground support, which has been determined from the system's constituent components. This comparison yields an expected level of damage when performed deterministically and can provide probabilities of different damage levels when performed stochastically by sampling the demand inputs. Overall, the expected damage was slightly more severe than the actual damage observed across the 2 cases. This can possibly be attributed to the conservative way pre-existing damage/burden is expected to load support during a strainburst. It has been assumed that the burden is incompressible and moves at the same velocity as the bursting volume, leading to a high energy demand on support. In practice, the burden may be compressible, which would lead to a reduced average velocity (and therefore energy demand). This is something that can be explored further in future work. It would also be beneficial to validate key demand parameters using independent observations (e.g. test holes, extensometers, and load cells).

References

Kaiser, P 2016, 'Ground support for constructability of deep underground excavations - challenges of managing highly stressed ground in civil and mining projects', *Sir Muir Wood lecture of International Tunnelling Association at World Tunnelling Congress*.

Kaiser, PK, McCreath, D & Tannant, D 1996, *Canadian Rockburst Support Handbook*, Geomechanics Research Center, Sudbury.

Kaiser, P & Moss, A 2022, 'Deformation-based support design for highly stressed ground with a focus on rockburst damage mitigation', *Journal of Rock Mechanics and Geotechnical Engineering*, vol. 14, no.1, pp. 50–66.

Malovichko, D 2020, 'Description of seismic sources in underground mines: theory', *Bulletin of the Seismological Society of America*, vol. 110, pp. 2124–2137.

Malovichko, DA 2022, 'Utility of seismic source mechanisms in mining', *Proceedings of the Tenth International Symposium on Rockbursts and Seismicity in Mines*, Society for Mining, Metallurgy & Exploration, Englewood.

Malovichko, D & Rigby, A 2022, 'Description of seismic sources in underground mines: dynamic stress fracturing around tunnels and strainbursting', *arXiv*, https://doi.org/10.48550/arXiv.2205.07379

Perras, MA & Diederichs, MS 2016, 'Predicting excavation damage zone depths in brittle rocks', *Journal of Rock Mechanics and Geotechnical Engineering*, vol. 8, no. 1, pp. 60–74.

Rigby, A 2024, 'Physically motivated moment-tensor decomposition for mining-induced seismicity', *Geophysical Journal International*, vol. 236, no. 1, pp. 443–455.

Rigby, A, Malovichko, D, Moridi, M & Kaiser, PK 2026a, 'Estimating bulking factor for rock around tunnels using LiDAR data', in *Proceedings of the Australian Conference on Rock Mechanics*, Australian Geomechanics Society, Brisbane, pp. 422–429.

Rigby, A, Malovichko, D & Kaiser, PK 2026b, 'A Rockburst Hazard Assessment Framework for Strainbursting', *Rock Mechanics and Rock Engineering*.